When Nanoparticles Meet Poly(Ionic Liquid)s: Chemoresistive CO_2 Sensing at Room Temperature

*Christoph Willa, Jiayin Yuan, Markus Niederberger, and Dorota Koziej**

Tetraalkylammonium-based poly(ionic liquid)s (PILs) are able to absorb particularly large amounts of CO_2; thus are considered up-and-coming materials in applications ranging from sensing, separation, to storage of CO_2. To meet the requirements of practical usage, their chemical activity has to be combined with other functionalities, for example, by fabricating composite materials. Poly[(*p*-vinylbenzyl)trimethylammonium hexafluorophosphate] and $La_2O_2CO_3$ nanoparticles—both of which are intrinsically insulating materials—are utilized as building blocks, taking full advantage of the electrostatic interaction at their interface to boost the overall conductivity of composites at room temperature. To rationalize this unique behavior, the charge transport mechanism is studied using impedance spectroscopy. It is found find that, for the composites with $La_2O_2CO_3$ content of 60–80 wt%, the interfacial effect becomes dominant and leads to the formation of conduction channels with increased mobility of $[PF_6]^-$ anions. These composites show further increase of the conductivity when exposed to pulses of CO_2 between 150 and 2400 ppm at room temperature in a relative humidity of 50%. This work therefore provides a simple strategy to achieve an enhancement of the electrical properties required for the utilization of PILs-based CO_2 sensors, but in the future this concept can be easily extended to other electronic devices.

1. Introduction

Polymer–inorganic composites are fascinating materials that play a large role in sustainable technologies for energy and environmental applications spanning from batteries, catalysts, fuel cells to gas sensors.[1–7] Their unique chemical reactivity and electrical properties have revolutionized new materials and devices.[8,9] In 1980s, gas sensor research embraced electron conducting polymers, laying the foundation for new sensor concepts,[10,11] which previously had been completely dominated by metal-oxide based sensors.[12–15] Unlike conventional gas sensors, sensors based on conductive polymer–inorganic nanoparticles are sensitive to oxidizing or reducing gases while operating at room temperature (RT).[16–18] Since then, electron conductive polymer-based sensors have attracted rapidly growing interest.[19] Particularly, the polymers with amino groups have been reported as promising candidates for CO_2 sensing, but in practice they suffer from poisoning with carbamates and therefore failed to fill the gap in the CO_2 gas sensor sector.[20,21] As a consequence, sensing of inert CO_2 gas is still performed with infrared spectroscopy, owing to trade-offs between the technological and economical factors, and having limited portability. Recently, poly(ionic liquid)s (PILs), a unique type of functional polyelectrolytes composed of ionic liquid repeating units chosen from structural diversity of the cation/anion-repertoire of ionic liquid chemistry, have been synthesized.[22–24] Their physical properties can be easily and broadly adjusted by the choice of the anion–cation pair. For example, structurally well-designed PILs are capable of reversible CO_2 capture and are showing high interfacial activity to bind various surfaces of metals, carbons, and to ionically interact with charged species via electrostatic repulsion or complexation.[25–28]

Others demonstrated the ability of resistive CO_2 sensing with carbon nanotubes (CNTs) wrapped with poly[1-(p-vinylbenzyl)-3-methyl-imidazolium tetrafluoroborate], P[VBTMA][BF_4].[29] They show a high sensitivity to low concentrations of CO_2 in oxygen-free atmospheres, but the response saturates already at 50 ppm, which is much lower than the normal CO_2 concentration level in fresh air (250 ppm) and thus lacks of practical application. Therefore, transforming the CO_2 sorption capacity of PILs into a chemoresistive sensor operating in real conditions, i.e., 21 vol% of oxygen and 50% relative humidity (rh), in the presence of 400 ppm[30] of CO_2 at RT requires a new structural model and additionally an understanding of the intrinsic interaction between organic and inorganic building blocks and their impact on the overall properties of such composites. Among different candidates, poly[(*p*-vinylbenzyl)-trimethylammonium hexafluorophosphate] P[VBTMA][PF_6] has an outstanding CO_2 adsorption capacity and high reversibility. This is possible because sp^3-hybridized tetraalkylammonium rearranges to accommodate CO_2.[31] Among different inorganic nanoparticles, only lanthanide-oxycarbonates show pronounced sensitivity to CO_2 but only at elevated working

C. Willa, Prof. M. Niederberger, Dr. D. Koziej
Laboratory for Multifunctional Materials
Department of Materials
ETH Zurich
Vladimir-Prelog-Weg 5, 8093 Zurich, Switzerland
E-mail: dorota.koziej@mat.ethz.ch
Dr. J. Yuan
Max-Planck Institute of Colloids and Interfaces
Am Mühlenberg 1, 14476 Potsdam, Germany

DOI: 10.1002/adfm.201500314

temperatures.[32,33] Moreover, it is difficult to fabricate resistive type CO_2 sensors, mainly due to the fact that both PILs and $La_2O_2CO_3$ exhibit intrinsically low electrical conductivity at RT.

In this work, we design composites that render possible the transduction of chemical reactivity of P[VBTMA][PF_6] and $La_2O_2CO_3$ into electrical signal at ambient conditions. Instead of simply using highly conductive inorganic fillers, i.e., Au[34] or CNTs,[29] we engineer highly conductive channels localized at the interface between P[VBTMA][PF_6] and $La_2O_2CO_3$ nanoparticles. A key aspect of our approach is precise tuning of the conductivity of the composites by taking advantage of the synergistic interaction at the interface between P[VBTMA][PF_6] and $La_2O_2CO_3$ nanoparticles. The impedance spectroscopy study presented here allows for separating the electrical contribution of the individual components and pins down the compositions, where the formation of the conductive channels at the interface between P[VBTMA][PF_6] and $La_2O_2CO_3$ nanoparticles are the most significant. Moreover, we show the benefits of applying such composites for CO_2 sensing at RT.

2. Results and Discussion

2.1. Fabrication of Composite Films

To manufacture composite films we use a classical approach of drop-casting shown in **Figure 1**a. $La_2O_2CO_3$ nanoparticles are dispersed in a homogenous solution of P[VBTMA][PF_6] in acetonitrile with intermittent sonication steps. As-prepared dispersions are stable over 4 h. The dispersion volume used in coating is optimized to maintain the thickness of films independent of their compositions. We dry the drop-casted films at 60 °C for 12 h to remove acetonitrile. We prepare six such composites, with $La_2O_2CO_3$ contents ranging from 0 to 100 wt%. The individual components are homogeneously distributed at the μm scale as shown in the scanning electron microscopy (SEM) images and energy dispersive x-ray (EDX) analysis maps of La and P in Figure 1b–d. Additionally, we find that the thickness of the films is in the range of 430 ± 50 nm. Further details are given in the Experimental Section and Supporting Information, Figures S1–S5.

2.2. Conductivity Channels at the Interface between $La_2O_2CO_3$ and P[VBTMA][PF_6]

To understand the interaction between the polymer and nanoparticles we use electrochemical impedance spectroscopy (EIS). We measure composites of $La_2O_2CO_3$ nanoparticles with contents of 0, 45, 60, 70, 80, and 100 wt%. We then fit the impedance spectra shown in **Figure 2**a with a $CPE_1|(R\text{-}CPE_2)$ Debye relaxator.[35,36] The constant phase element CPE_1 represents the dielectric bulk capacitance, whereas the conduction path consists of a resistor R in series with CPE_2. CPE_2 models charge carrier diffusion in composite material, and thus in pure samples (0 and 100 wt% $La_2O_2CO_3$) R-CPE_2 reduces to a single resistor.[36] Figure 2b illustrates the dependence of R, CPE_1, and CPE_2 as a function of film composition. The impedance of a CPE is defined by Q and α as $Z_{CPE} = (Q(i\omega)^{\alpha})^{-1}$. Strikingly, R decreases by over one order of magnitude for composites of 60–80 wt% $La_2O_2CO_3$, although the inorganic compound is an isolator. Since the ammonium cations are immobilized on the polymer chain, it is mainly the $[PF_6]^-$ anions that contribute to ionic conductivity. The surface of metal oxycarbonate nanoparticles in ambient conditions is usually covered with negatively charged species.[32] Therefore, we believe that the surface charges of the nanoparticles interact electrostatically with the ammonium cation of the polymer resulting in increased anion mobility near the particle surface as shown in Figure 2c. If the concentration of both the polymeric and the inorganic phase is precisely tuned to create the maximum interface, the formation of such ionic channels is enabled, and they become a dominant conductivity path, explaining the drop of the overall resistance of the films. Figure 2d illustrates schematically this behavior. A similar phenomenon has been reported recently for SiO_2-P[VBTMA][BF_4] and SiO_2-LiI/3-hydroxypropionitrile composites.[6,37] CPE_1 remains almost unchanged as it only depends on the sample geometry and relative permittivity of the materials. In fact, ε_r is particularly large for ammonium cation based PILs[38] and can reach values larger than 10 for some PILs.[39] These values are comparable to ε_r-values of $La(OH)_3$ or La_2O_3,[40,41] explaining the minor variations in CPE_1. The term α_2 varies around 0.5, indicating an infinite length Warburg element and confirming the influence of diffusion effects. An infinite

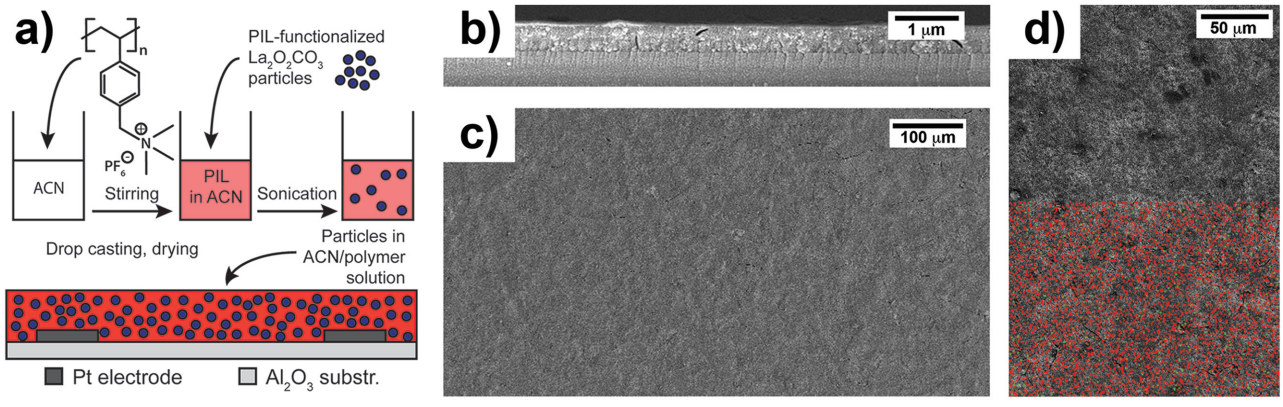

Figure 1. a) Fabrication procedure of the composite films; SEM images of films composed of 70 wt% of $La_2O_2CO_3$ and 30 wt% of P[VBTMA][PF_6], b) cross-section view, c) top-view, d) top-view and maps of elemental distribution of lanthanum (green) and phosphorus (red). ACN stands for acetonitrile.

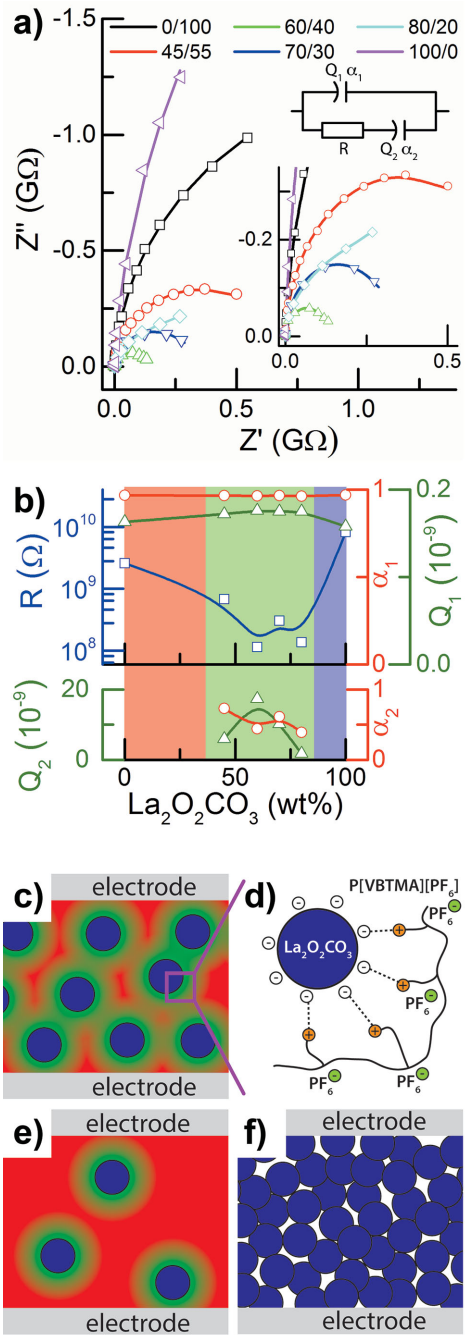

Figure 2. a) Nyquist plots of composites composed of 0, 45, 60, 70, 80, and 100 wt% of $La_2O_2CO_3$ in P[VBTMA][PF_6]; (inset) an equivalent electrical circuit. Measured data (hollow symbols), fitted curve (solid line). b) Fit parameters of R, CPE_1, and CPE_2 as a function of $La_2O_2CO_3$-content. c,d) Schematic drawing illustrating the formation of the conductivity channels (green) at the interface between $La_2O_2CO_3$ (blue) and P[VBTMA][PF_6] (red); (not in scale). e,f) Schematic of the composites with $La_2O_2CO_3$ content below 40 and above 80 wt%, respectively.

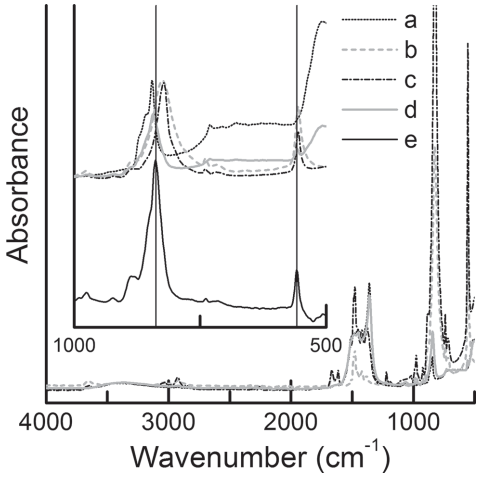

Figure 3. ATR IR spectra of a) $La_2O_2CO_3$, b) P[VBTMA][PF_6], c) 45 wt% $La_2O_2CO_3$ in P[VBTMA][PF_6], d) washed $La_2O_2CO_3$ nanoparticles with P[VBTMA][PF_6] noncovalently bonded to the surface. Inset shows all spectra in the wavenumber region characteristic for ν(PF) vibration, which partially overlaps with the region characteristic of $\nu_2(CO_3^{2-})$ vibrations. For the sake of comparison all spectra are rescaled that the overlapping vibrations at 830 cm^{-1} are of the same height. e) A differential spectrum of d) and a) spectra allows to eliminate the aforementioned overlap. The spectrum shows only the species at the surface of $La_2O_2CO_3$ nanoparticles.

length Warburg element occurs when the layer is too thick to be penetrated completely by the $[PF_6]^-$ anions even at the lowest alternating current (AC) frequency. Also, Q_2 increases for 60 and 70 wt% particle content owing to the increased anion-mobility at the particle–polymer interface and decreasing the overall Warburg coefficient.[42] For the composites with $La_2O_2CO_3$ content below 40 and above 80 wt% the intrinsic properties of individual components surpass the interfacial effects as schematically shown in Figures 2e and 2f for P[VBTMA][PF_6] and $La_2O_2CO_3$, respectively. The morphology of pure $La_2O_2CO_3$ film is shown in Supporting Information, Figure S5.

To verify the type of interaction between PIL and $La_2O_2CO_3$, we compare the attenuated total reflectance (ATR IR) spectrum of the composites with the spectra of individual components shown in **Figure 3**, spectra a–c. In general, the surface of metal oxycarbonate nanoparticles in ambient conditions is covered with intrinsically negatively charged carbonates and additionally with adsorbed water, hydroxyl groups, and oxygen ions.[32] The lack of new bands or shifting of the existing bands in the spectrum of composites points to the noncovalent character of interaction between the surface of $La_2O_2CO_3$ nanoparticles and P[VBTMA][PF_6]. To further estimate the strength of interaction we check if we can fully remove the polymer from the surface of nanoparticles by thorough, repeated washing in acetonitrile. For more details see the Experimental Section and Supporting Information, Figures S6–S8. The bands corresponding to the asymmetric and symmetric vibration of ν(PF) at 825 and 555 cm^{-1}, respectively, are still visible in the ATR IR spectrum of washed particles as shown in Figure 3 and Figure 3 inset, spectrum d. The differential spectrum e, between $La_2O_2CO_3$ (spectrum a) and of the washed nanoparticles (spectrum d) further emphasizes the ν(PF) vibrations. Moreover, elemental analysis confirms the presence of P, F, and N at the surface of nanoparticles as shown in the Supporting Information. Therefore, we conclude that P[VBTMA][PF_6] noncovalently binds to the surface of lanthanum oxycarbonate by strong electrostatic

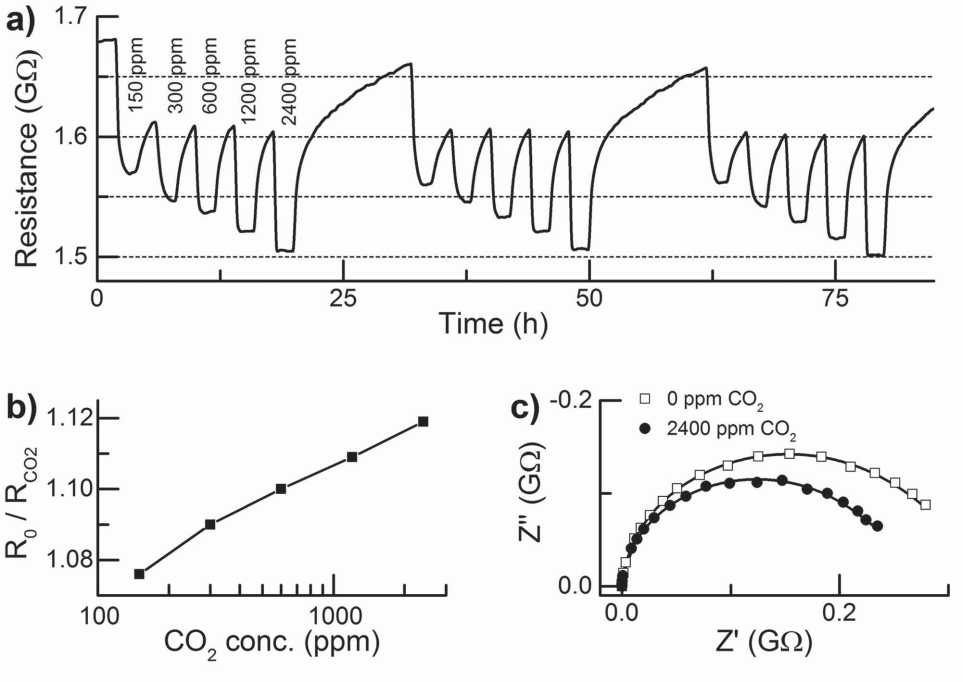

Figure 4. Sensing performance of films composed of 70 wt% $La_2O_2CO_3$ at 50% rh in air and at RT. a) DC resistance changes during exposure to CO_2 pulses between 150 and 2400 ppm. b) Corresponding sensor signal, calculated as resistance in air divided by resistance under CO_2. c) Nyquist plots with (circles) and without (squares) 2400 ppm CO_2. Measured data (symbols), fitted curve (solid line).

interaction of the ammonium cation with the negatively charged surface of $La_2O_2CO_3$ as illustrated in Figure 2c.

2.3. CO_2 Sensing at Ambient Conditions

We assess CO_2 sensing performance of composite layers with 70 wt% content of $La_2O_2CO_3$ by monitoring their direct current (DC) resistance changes upon exposure to different pulses of CO_2, in the concentration range relevant for indoor air quality monitoring, at RT and 50% rh as shown in **Figure 4**a. For three consecutive CO_2 sensing experiments, each one composed of five CO_2 pulses between 150 and 2400 ppm, we obtain the absolute resistance changes on the order of hundreds of megaohms. We define, similar to metal-oxide based gas sensors,[12] the sensor signal as the resistance of the sensor in air (R_0) divided by the sensor resistance under exposure to CO_2 (R_{CO2}) as shown in Figure 4b. The response time is defined as the time it takes to reach 90% of the sensor signal for a given CO_2 concentration. The determination of the response and recovery time is illustrated in Supporting Information, Figure S9, and values for each concentration are given in Supporting Information, Table S1. We note that the recovery time is much slower than the response time; between the CO_2 pulses, the resistance does not fully recover to the initial R_0 value. Therefore, to calculate the sensor signal we use the initial value of R_0 and not the value immediately before the individual CO_2 pulses. Nevertheless, the absolute resistance under CO_2 (R_{CO2}), for a given CO_2 concentration is always the same (<0.1%), independent of the baseline resistance directly before the CO_2 pulse. This suggests that the sensor is potentially independent of the drift of the baseline resistance, which is for instance a main drawback of chemoresistive metal-oxide-based gas sensors.

However, the sensing mechanism of P[VBTMA][PF_6]/$La_2O_2CO_3$ based sensors appears to be different than semiconductor-based sensors operated at elevated temperatures; thus, in the following we will refrain from their direct comparison. Instead we find it helpful to analyze the CO_2 sensing performance of previously reported PILs/CNTs-based sensors.[29] The reported resistance changes due to exposure to even smaller CO_2 concentrations are irreversible and their recovery has to be triggered by an additional UV irradiation step. Additionally, unlike PIL/CNTs- and polyethylenimine-based sensors,[21,29] the P[VBTMA][PF_6]/$La_2O_2CO_3$ sensors show instead of an increase a decrease of resistance upon exposure to CO_2, which indicates a fundamentally different reaction mechanism. To assess the origin of this discrepancy we investigate the influence of CO_2 on the impedance spectra of the composite as shown in Figure 4c. We record the impedance data in a quasi-equilibrium condition; it means that the sensor signal to 2400 ppm of CO_2 reached the saturation value. We fit the spectra with the $CPE_1|(R\text{-}CPE_2)$ model and find that the CO_2 exposure induces indeed a decrease of resistance R assigned to the conductivity channels at the interface between P[VBTMA][PF_6] and $La_2O_2CO_3$. A plausible explanation is that the sp^3-hybridized tetraalkylammonium rearranges to accommodate CO_2,[31] thus interacting less with the anion and giving rise to the increased mobility of the $[PF_6]^-$ anion and increased conductivity of the composites.

3. Conclusions

Here we present a straightforward approach to fabricate conductive composite films composed of $La_2O_2CO_3$ and a poly(ionic liquid), P[VBTMA][PF_6]. We show that the electrostatic interaction of P[VBTMA][PF_6] with negatively charged $La_2O_2CO_3$ enables higher mobility of $[PF_6]^-$ anions nearby the nanoparticle surface and increases the overall conductivity of the composites. The interface phenomenon becomes dominant in the concentration range of $La_2O_2CO_3$ between 60 and 80 wt% and leads to the formation of conductivity channels. The composites with 70 wt% $La_2O_2CO_3$ show a decrease in resistance when exposed to CO_2 at RT and in humid conditions. This behavior is unique among previously reported polymer-based CO_2 sensors, and suggests that the underlying mechanism is not related to the formation of bicarbonate or carbamate species. Moreover, our AC impedance studies leave no doubt that the increased conductivity of the composites and the increase in conductivity under CO_2 are related to the same mechanism. Currently our data points toward that the rearrangement of tetraalkylammonium cations in the presence of CO_2 leads to increased mobility of $[PF_6]^-$ anions. This hypothesis needs further verification, for example by a study of the non-covalent interaction between $La_2O_2CO_3$ and P[VBTMA][PF_6] with near-edge x-ray absorption fine-structure spectroscopy[43] or mapping of the surface potential distribution by Kelvin probe force microscopy.[44] The results from this study will then trigger innovation in engineering materials based on PIL-inorganic nanoparticles ranging from sensing, separation to storage of CO_2.[45]

4. Experimental Section

Chemicals: La(O^iPr)$_3$ (Strem Chemicals, 99%), acetophenone (Fluka, >99%), acetone (Sigma-Aldrich, >99.9%), acetylacetone (Fluka, >99.5%), 1-hexanol (Acros, 98%), 2-propanol (Fluka, >99.8%), hydroxypropyl cellulose with $\bar{M}_w \approx 80\,000$ (Aldrich, 99%), acetonitrile (Sigma-Aldrich, >99.5%), 4-vinylbenzyl chloride (Sigma-Aldrich, 90%), 2,6-di-tert-butyl-4-methylphenol (Sigma-Aldrich, 99%), trimethylamine (Sigma-Aldrich, 31–35 wt% in ethanol), ethanol (VWR, analytical grade), diethyl ether (VWR, analytical grade), potassium hexafluorophosphate (Sigma-Aldrich, 98%) dimethylformamide (VWR, analytical grade), 2,2'-azobis(2-methylpropionitril) (Sigma-Aldrich, 98%), and methanol (VWR, analytical grade) were used as received without further purification.

$La_2O_2CO_3$Nanoparticles: To fabricate La(OH)$_3$ nanoparticles we adapted a previously reported synthesis.[33] In a typical synthesis 0.5 mM(158.1 mg) of La(O^iPr)$_3$ were dissolved in 40 mM (4.67 mL) of acetophenone, mixed under Ar atmosphere in a 10 mL pressure vial and stirred for 10 min. The ocher, transparent solution was sealed and heated in a CEM Explorer microwave at 200 °C for 20 min. Subsequently, the precipitate was extracted by centrifugation and washed three times with acetone. The nanoparticles were dried in a lab furnace at 60 °C overnight. We obtained 11 nm large $La_2O_2CO_3$ nanoparticles via calcination of La(OH)$_3$ nanoparticles at 400 °C for 2 h. The detailed characterization of the nanoparticles is given in Supporting Information, Figures S1–S4.

Synthesis of p-Vinylbenzyltrimethylammonium Chloride: In a 250 mL flask, 4-vinylbenzyl chloride (31.0 g, 0.20 M) and inhibitor 2,6-di-tert-butyl-4-methylphenol (50 mg) were loaded. The mixture was cooled by ice water under nitrogen atmosphere. 71.6 g of trimethylamine (23.6 g, 0.40 M) solution in ethanol was then added. The mixture was stirred at RT for 24 h. Afterwards the mixture was concentrated by rotary evaporator and precipitated in 1 L diethyl ether. A white powder was obtained and dried under vacuum at RT till constant weight. Yield: 25.8 g, 60%. ^{1}H NMR (D_2O, 400 MHz, ppm): $\delta \approx 8.7$ (1H), 7.5 (2H), 7.4 (2H), 7.3 (2H), 6.6 (1H), 5.8 (1H), 5.3 (3H), 4.1 (2H), 1.8 (2H), 1.2 (2H), 0.8 (3H).

Synthesis of p-Vinylbenzyltrimethylammonium Hexafluorophosphate: p-vinylbenzyltrimethylammonium chloride (25.40 g, 0.12 M), potassium hexafluorophosphate (KPF_6) (24.30 g, 0.13 M), and DMF (150 mL) were mixed and stirred for 24 h at RT The solid white precipitate was filtered off. The filtrate was concentrated by rotary evaporation under vacuum at 70 °C to 80 mL. The newly appearing powder was filtered off again. The filtrate was dropped into IL diethyl ether. The white precipitate was collected and dried under vacuum till constant weight at RT (29.5 g, 80%). ^{1}H NMR (DMSO-d_6, 400 MHz, ppm) $\delta \approx 3.0$ (3Hs), 4.5 (2H), 5.3 (1H), 6.0 (1Hd), 4.3 (2H), 7.4 (2H), 9.5 (1H).

Synthesis of Poly[(p-vinylbenzyl)trimethylammonium Hexafluorophosphate], P[VBTMA][PF_6]: In a typical run, 3.0 g of [VBTMA][PF_6], 66 mg of 2,2'-azobis(2-methylpropionitril) (AIBN), and 7 mL of DMF were charged into a Schlenk flask. The flask was degassed and backfilled with argon 3 times. At the end, the flask was refilled with argon and immersed in an oil bath at 85 °C for 24 h. The solution was then cooled down and poured into methanol to precipitate out the polymer. After drying under vacuum at 80 °C, 2.5 g of polymer was obtained. Yield: 83%. ^{1}H NMR (DMSO-d_6, 400 MHz, ppm) 1.45 (2H), 2.85 (9H), 4.30 (2H), 6.41 (2H), 7.05(2H).

Sensor Fabrication: Synthesized $La_2O_2CO_3$ particles were added to a 25 mL centrifugation tube. After addition of the same amount of P[VBTMA][PF_6] and 20 mL acetonitrile, the dispersion was sonicated for 1 h. The tube was left to rest for another hour and 18 mL of the opaque dispersion were transferred to a second tube. Subsequently, PIL-functionalized particles were washed three times to remove buoyant PIL and dried in a 60 °C oven overnight. For different composition, particles were mixed with P[VBTMA][PF_6] in the desired ratio and acetonitrile is added to finally obtain a 50 mg mL^{-1} dispersion. Sensors are then manufactured by drop casting 7.5 mL on the alumina substrate equipped with interdigitated Pt electrodes. The pure $La_2O_2CO_3$ sample was calcined at 400 °C for 2 h to remove all organics from the surface. The morphology of $La_2O_2CO_3$ is shown in Supporting Information, Figure S5.

Materials Characterization: X-ray powder diffraction (XRD) patterns were measured on a PANalytical Empyrean powder diffractometer in reflection mode using Cu Kα radiation and operating at 45 kV and 40 mA. SEM images were taken on a LEO 1530 Gemini microscope operated at an acceleration voltage of 3 kV. The PIL-containing samples were coated with a 5 nm layer of sputtered Pt for the SEM imaging. EDX spectroscopy is performed on a Hitachi SU-70 operated at 20 kV acceleration voltage. An X-Max detector (semiconductor-type, Oxford Instruments) was used. For the transmission electron microscope (TEM) imaging, the samples were dispersed in acetone by sonication and a drop of the suspension was air-dried onto a carbon-coated copper grid.

Sensing Performance: Sensitivity toward CO_2 in humid air was tested in a continuous-flow chamber. A computer-controlled gas mixing system equipped with Bronkhorst mass flow controllers adjusts the gas concentrations at the constant flow of 200 mL min^{-1} in synthetic air as a carrier gas. To monitor changes of the DC resistance or of the AC impedance of the sensor during exposure to the target gases, the electrodes of the sensor were connected to a Keithley 617 electrometer or Zahner IM6 electrochemical workstation, respectively. AC impedance data were acquired in the frequency range from 0.79 Hz to 1 MHz; working conditions were RT and 50% rh.

Supporting Information

Supporting Information is available from the Wiley Online Library or from the author.

Acknowledgements

This work was supported by the ETH Zurich Research Grant No. ETH-2813-1. J.Y. thanks the HINT-COST action MP1202. We thank the Scientific Center for Optical and Electron Microscopy (SCOPEM) for access to the electron microscope facility and Dr. Martin J. Süess for taking the TEM images.

Received: January 25, 2015
Revised: February 19, 2015
Published online: March 16, 2015

[1] C. Sanchez, P. Belleville, M. Popall, L. Nicole, *Chem. Soc. Rev.* **2011**, *40*, 696.
[2] N. A. Kotov, I. Dékány, J. H. Fendler, *Adv. Mater.* **1996**, *8*, 637.
[3] B. C. H. Steele, A. Heinzel, *Nature* **2001**, *414*, 345.
[4] J. M. Tarascon, M. Armand, *Nature* **2001**, *414*, 359.
[5] T. C. Merkel, B. D. Freeman, R. J. Spontak, Z. He, I. Pinnau, P. Meakin, A. J. Hill, *Science* **2002**, *296*, 519.
[6] H. Wang, H. Li, B. Xue, Z. Wang, Q. Meng, L. Chen, *J. Am. Chem. Soc.* **2005**, *127*, 6394.
[7] T. Y. Kim, H. W. Lee, M. Stoller, D. R. Dreyer, C. W. Bielawski, R. S. Ruoff, K. S. Suh, *ACS Nano* **2010**, *5*, 436.
[8] A. C. Balazs, T. Emrick, T. P. Russell, *Science* **2006**, *314*, 1107.
[9] Y. Dzenis, *Science* **2008**, *319*, 419.
[10] A. Star, T. R. Han, V. Joshi, J. C. P. Gabriel, G. Grüner, *Adv. Mater.* **2004**, *16*, 2049.
[11] H. Bai, G. Shi, *Sensors* **2007**, *7*, 267.
[12] N. Barsan, U. Weimar, *J. Electroceram.* **2001**, *7*, 143.
[13] N. Barsan, D. Koziej, U. Weimar, *Sens. Actuators, B* **2007**, *121*, 18.
[14] E. Comini, G. Sberveglieri, *Mater. Today* **2010**, *13*, 36.
[15] G. Korotcenkov, *Sens. Actuators, B* **2005**, *107*, 209.
[16] H. Shiigi, T. Oho, T. Tonosaki, K. Ogura, *Electrochemistry* **2001**, *69*, 997.
[17] H. Yoon, J. Jang, *Adv. Funct. Mater.* **2009**, *19*, 1567.
[18] C. M. Hangarter, N. Chartuprayoon, S. C. Hernández, Y. Choa, N. V. Myung, *Nano Today* **2013**, *8*, 39.
[19] J. Janata, M. Josowicz, *Nat. Mater.* **2003**, *2*, 19.
[20] T. C. D. Doan, R. Ramaneti, J. Baggerman, J. F. van der Bent, A. T. M. Marcelis, H. D. Tong, C. J. M. van Rijn, *Sens. Actuators B* **2012**, *168*, 123.
[21] T. C. D. Doan, J. Baggerman, R. Ramaneti, H. D. Tong, A. T. M. Marcelis, C. J. M. van Rijn, *Sens. Actuators B* **2014**, *201*, 452.
[22] J. Texter, V. A. Vasantha, R. Crombez, R. Maniglia, L. Slater, T. Mourey, *Macromol. Rapid Commun.* **2012**, *33*, 69.
[23] J. Texter, *Macromol. Rapid Commun.* **2012**, *33*, 1996.
[24] D. England, L. Slater, T. Mourey, J. Texter, *ACS Macro Lett.* **2013**, *2*, 901.
[25] J. Tang, H. Tang, W. Sun, M. Radosz, Y. Shen, *J. Polym. Sci., Part A: Polym. Chem.* **2005**, *43*, 5477.
[26] J. E. Bara, S. Lessmann, C. J. Gabriel, E. S. Hatakeyama, R. D. Noble, D. L. Gin, *Ind. Eng. Chem. Prod. Res. Dev.* **2007**, *46*, 5397.
[27] A. Wilke, J. Yuan, M. Antonietti, J. Weber, *ACS Macro Lett.* **2012**, *1*, 1028.
[28] S. Soll, Q. Zhao, J. Weber, J. Yuan, *Chem. Mater.* **2013**, *25*, 3003.
[29] Y. Li, G. Li, X. Wang, Z. Zhu, H. Ma, T. Zhang, J. Jin, *Chem. Commun.* **2012**, *48*, 8222.
[30] P. Tans, Atmospheric CO_2 Concentration at Mauna Loa Observatory. http://www.esrl.noaa.gov/gmd/ccgg/trends/ (accessed January 23, 2015).
[31] S. Supasitmongkol, P. Styring, *Energy Environ. Sci.* **2010**, *3*, 1961.
[32] I. Djerdj, A. Haensch, D. Koziej, S. Pokhrel, N. Barsan, U. Weimar, M. Niederberger, *Chem. Mater.* **2009**, *21*, 5375.
[33] A. Haensch, D. Koziej, M. Niederberger, N. Barsan, U. Weimar, *Procedia Eng.* **2010**, *5*, 139.
[34] S. Lee, M. D. Cummins, G. A. Willing, M. A. Firestone, *J. Mater. Chem.* **2009**, *19*, 8092.
[35] I. D. Raistrick, D. R. Franceschetti, J. R. Macdonald, *Impedance Spectroscopy: Theory, Experiment, and Applications*, John Wiley & Sons, Inc., Hoboken, New Jersey **2005**.
[36] V. F. Lvovich, *Impedance Spectroscopy: Applications to Electrochemical and Dielectric Phenomena*, John Wiley & Sons, Inc., Hoboken, New Jersey **2012**.
[37] P. Wang, Y.-N. Zhou, J.-S. Luo, Z.-H. Luo, *Polym. Chem.* **2014**, *5*, 882.
[38] J. Tang, M. Radosz, Y. Shen, *Macromolecules* **2008**, *41*, 493.
[39] Y. Dong, J. Yin, X. Zhao, *J. Mater. Chem. A* **2014**, *2*, 9812.
[40] H. Yamada, T. Shimizu, A. Kurokawa, K. Ishii, E. Suzuki, *J. Electrochem. Soc.* **2003**, *150*, G429.
[41] Y. Zhao, M. Toyama, K. Kita, K. Kyuno, A. Toriumi, *Appl. Phys. Lett.* **2006**, *88*, 072904.
[42] A. J. Bard, L. R. Faulkner, *Electrochemical Methods: Fundamentals and Applications*, John Wiley & Sons, Inc., Hoboken, New Jersey **2001**.
[43] A. D. Winter, E. Larios, F. M. Alamgir, C. Jaye, D. A. Fischer, M. Omastová, E. M. Campo, *J. Phys. Chem. C* **2014**, *118*, 3733.
[44] H. O. Jacobs, P. Leuchtmann, O. J. Homan, A. Stemmer, *J. Appl. Phys.* **1998**, *84*, 1168.
[45] S. Li, Z. Wang, X. Yu, J. Wang, S. Wang, *Adv. Mater.* **2012**, *24*, 3196.